

# Combined spacecraft stabilization control after multiple impacts during the capture of a tumbling target by a space robot

Dong Han<sup>a,b</sup>, Panfeng Huang<sup>a,b,\*</sup>, Xiyao Liu<sup>a,b</sup>, Yang Yang<sup>a,b</sup>

<sup>a</sup> National Key Laboratory of Aerospace Flight Dynamics, Northwestern Polytechnical University, Xi'an, 710072, China

<sup>b</sup> Research Center for Intelligent Robotics, School of Astronautics, Northwestern Polytechnical University, Xi'an, 710072, China

## ARTICLE INFO

### Keywords:

Space robot  
Multiple impacts  
Dual-integral sliding mode control  
Combined spacecraft stabilization

## ABSTRACT

Target capture is a fundamental and essential task of space robots for on-orbit servicing in the future. Accordingly, it is important to study the method for space robot stabilization after impact during target capture. In this paper, the stabilization control problem of a combined spacecraft after multiple impacts during target capture is studied. A dual-integral sliding mode (DISM) control method based on the reconfiguration of the reaction wheels is proposed. The stability control of the combined spacecraft is achieved by controlling the reaction wheels of the space robot to absorb the angular momentum arising from the impact. First, given the structure of the gripper, the contact detection algorithm and contact dynamics model are established, and then multiple impacts are simulated during the target capturing operation. Second, an improved sliding mode control method is proposed to overcome the influence of multiple impacts, and the stability of the controller is confirmed by the Lyapunov method. Third, through an optimization method, the configuration of the reaction wheels of the space robot is reconstructed to avoid control torque saturation. The validity and availability are eventually verified by simulations and experiments. The results show that the proposed method can achieve the stability of the combined spacecraft after the target capture, and the algorithm is robust and has engineering applicability.

## 1. Introduction

The space robot is an effective device for performing spacecraft on-orbit servicing tasks. It can perform such tasks as on-orbit refueling, maintenance, equipment replacement, and debris removal [1–4]. In order to complete the on-orbit servicing mission, it is necessary to first capture the failed spacecraft. The capture process is generally divided into four phases [5], namely, observation and estimation, proximity and docking, target capture (physical interception), and stability control of the combined spacecraft. In order to reduce the impact of the collision, researchers proposed research focused on three relevant aspects. The first objective is to make the end effector and the target's grasped fixture have a relative velocity of zero. A prediction and motion-planning scheme, which ensures that the relative velocity between the target and the capturer is zero and avoids collision, has been previously proposed [6]. Considering the noise of the sensor and the hysteresis of the mechanical system, such scheme is difficult to implement in practice. Other scholars have studied non-contact de-spinning of a space object in an effort to de-tumble the rotating target and achieve the contact-free capture [7–10]. However, these approaches are not yet

developed to the point that they can be implemented in practice and are only in the theoretical verification stage. The second objective is to preload the bias momentum in the space robot system [11,12], absorbing the target momentum with the manipulator. The third objective is to develop a control method to reduce the disturbance caused by the contact force. Liu [13] studied the linear control of the manipulator joints to achieve the stability of the robot system after target capture. Zhang [14] proposed an improved adaptive sliding mode control algorithm to stabilize a non-cooperative target with a large inertia. Stolfi [15] investigated a combined impedance-PD method to maintain a stable contact between the end-effector and the target. Others have developed an optimal control strategy to minimize the contact force on the servicing satellite [16,17]. Also, impedance control has been proposed to minimize the contact force by controlling the position/force of the end-effector [18,19]. However, due to the execution speed of the end-effector and the limitation of measurement accuracy, the collision cannot be avoided. Little research has been reported on the multiple impact problems that occur during the experiment. Therefore, it is necessary to study the characteristics of multiple impacts and the stabilization control after collision.

\* Corresponding author. National Key Laboratory of Aerospace Flight Dynamics, Northwestern Polytechnical University, Xi'an, 710072, China.

E-mail address: [pfhuang@nwpu.edu.cn](mailto:pfhuang@nwpu.edu.cn) (P. Huang).

<https://doi.org/10.1016/j.actaastro.2020.05.035>

Received 5 November 2019; Received in revised form 2 April 2020; Accepted 18 May 2020

Available online 06 June 2020

0094-5765/ © 2020 IAA. Published by Elsevier Ltd. All rights reserved.

A few studies have been reported on the stability of the combined spacecraft with structural mutations. For instance, Cyril [20] proposed the idea of coordinated control of robotic arms and reaction wheels, using the “Bias Momentum Control” and “Distributed Momentum Control” methods to achieve the stable control of the combined spacecraft after the target capture. Another study [21] proposed achieving the stability of the combined body and the repositioning of the target using the motion of the robot manipulator. Roithmayr [22] studied the spacecraft torque equilibrium attitude (TEA) control problem using the flywheels and a control moment gyroscope (CMG) as the implementing agent, and the linear quadratic regulator (LQR) method to design the spacecraft’s TEA stabilization controller. Wei [23] introduced a low-complexity preset performance control method that does not require a priori estimation or on-line identification of the specific parameters of the model. By presetting the performance indicators of the system, a stable control is achieved under unknown system parameters. Another study proposed an improved State-dependent Riccati equation (SDRE) optimal controller to guarantee the convergence of the steady-state position errors and velocity errors [24]. In addition, the tether was introduced to eliminate the influence of the angular momentum after contact and to solve the possible actuators saturation problem [25].

Considerable work has been carried out on the contact control and post-capture stability system design by various researchers. However, little research focuses on the analysis of collision process and the impact on stability of combined spacecraft. An approach is proposed in this paper to achieve post-capture stability control of the combined spacecraft after collision. Evidently, the control system design is quite challenging and complicated, and it mainly reflects in the following three aspects:

- 1) Collision modeling and analysis are considered in post-capture phase, with the goal of eliminating the impact of collision on combined spacecraft through the design of a stabilization controller.
- 2) For the multiple impacts generated in the experiments, the control system requires a control algorithm for a faster response and greater robustness.
- 3) To deal with the sudden changes in the quality characteristics of the space robot caused by the capture of the target, the reconfiguration of the reaction wheels and re-allocation of the control torque are required.

This paper is organized as follows: In Section 2, the dynamics of the combined spacecraft and contact dynamics are established in terms of the Kelvin model, and the multiple impact detection algorithm is proposed. In Section 3, an improved sliding mode controller is designed, the stability of the control scheme is analyzed and proven, and then the control redistribution based on a Moore-Penrose inverse technique is introduced. In addition, in Section 4, the contact experiments and numerical simulations are conducted to verify the effectiveness of the approach. Finally, the conclusions are given in Section 5.

## 2. Attitude dynamics of the combined spacecraft and contact dynamics

### 2.1. Problem description

In order to improve the attitude stability of the spacecraft, a flywheel three-axis attitude stabilization system is widely used for a spacecraft in middle and high altitude orbits. This paper studies the stability control of the post-contact composite spacecraft using the flywheel three-axis attitude stabilization system of the space robot. The composite spacecraft mainly includes the space robot (including the space base and manipulators) and the captive target, and its structure is illustrated in Fig. 1.

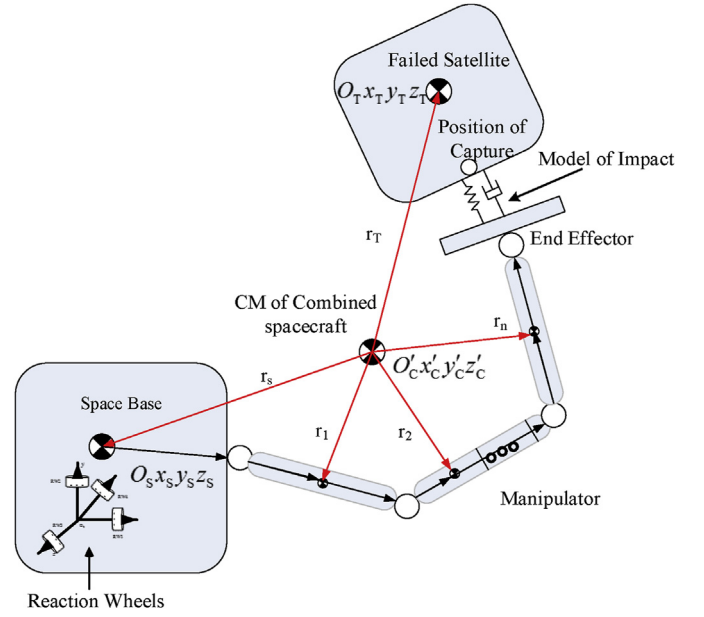


Fig. 1. Illustration of contact and capture.

### 2.2. Attitude dynamics and kinematics

The inertial parameters and inertia axis of the combined spacecraft are different from those of the space robot before capture, which affects the three-axis attitude stabilization system of the space robot. Therefore, the inertial parameters and inertia axes of the combined spacecraft need to be calculated.

**Assumption 1.** The grasping point and mass characteristics of the space robot, manipulators and captured target are known or can be obtained by means of identification.

Defining the inertia matrix of the combined spacecraft as expressed in the body frame of the combined spacecraft coordinated  $I^*$ , as shown in Fig. 1, then its formula is given by:

$$I^* = R_S I_S R_S^T + m_S [(r_S^T r_S) E_3 - r_S r_S^T] + R_T I_T R_T^T + m_T [(r_T^T r_T) E_3 - r_T r_T^T] + \sum_{i=1}^n R_i I_i (R_i)^T + m_i [(r_i^T r_i) E_3 - r_i (r_i)^T] \quad i = 1, 2, \dots, n \quad (1)$$

where  $m_S$ ,  $m_T$  and  $m_i$  are the mass of the servicing spacecraft, target satellite and the  $i$  th link of the manipulator, respectively;  $r_S$ ,  $r_T$  and  $r_i$  are the centroid position vectors of space robot, target satellite and the  $i$  th link of manipulator, respectively;  $I_S$ ,  $I_T$  and  $I_i$  are the inertia tensor of space robot, target satellite and the  $i$  th link of manipulator, respectively;  $R_S$ ,  $R_T$  and  $R_i$  are the attitude rotation matrix of space robot, target satellite and the  $i$  th link of manipulator, respectively;  $I^*$  denotes the  $I$  identity matrix.

The inertia matrix of the combined spacecraft is defined as in the inertia principal axis coordinate  $O_C x_C y_C z_C$ ;  $\Phi$  is the transformation matrix of the combined spacecraft body coordinate  $O'_C x'_C y'_C z'_C$  to the inertia principal axis coordinate  $O_C x_C y_C z_C$ ;  $\rho'$  and  $\rho$  are respectively the mass element position vector of the two coordinate systems. The relationship between the two is given by:

$$\rho = \Phi \rho' \quad (2)$$

Therefore, the inertia matrix transformation between the two coordinate systems is given by

$$I = \int (\rho'^T \rho' E - \rho' \rho'^T) dm = \int (\rho'^T \Phi^T \Phi \rho - \Phi \rho \rho^T \Phi^T) dm = \Phi I^* \Phi^T \quad (3)$$

where  $\Phi$  is the orthogonal transform matrix and  $\Phi\Phi^T = \Phi^T\Phi = \mathbf{E}$ .

Considering that the space robot has four reaction wheels for attitude stabilization, the angular momentum of the combined spacecraft in the inertial spindle coordinate system can be expressed as:

$$\mathbf{H} = \mathbf{I}\omega + \mathbf{C}\mathbf{J}_w\Omega \quad (4)$$

where  $\mathbf{J}_w$  is the inertia matrix of reaction wheels,  $\Omega$  is the reaction wheels angular velocity vector,  $\Omega = [\Omega_1, \Omega_2, \Omega_3, \Omega_4]^T$ ,  $\mathbf{C}$  is the reaction wheel configuration matrix,  $\omega$  is the absolute angular velocity expressed in the inertia frame.

Since the collision occurs before the target is captured, considering the short contact time and the large contact torque, the effects of the gravity gradient torque and aerodynamic torque can be neglected. The Euler dynamic equation of the reaction wheel is given:

$$\mathbf{J}_s\dot{\omega} = -\omega \times (\mathbf{I}\omega + \mathbf{C}\mathbf{J}_w\Omega) + \mathbf{C}\mathbf{u}_w + \mathbf{T}_c \quad (5)$$

$$\mathbf{J}_w(\dot{\Omega} + \mathbf{C}^T\dot{\omega}) = \mathbf{u}_w \quad (6)$$

where  $\mathbf{J}_s = \mathbf{I} - \mathbf{C}\mathbf{J}_w\mathbf{C}^T$ ,  $\mathbf{u}_w$  is the input torque, and  $\mathbf{T}_c$  is the contact torque.

According to Eq.(4) and (5) and (6), a nonlinear combined spacecraft attitude dynamics equation containing the reaction wheels can be obtained as follows:

$$\begin{cases} \dot{\omega} = \mathbf{J}_s^{-1}[\omega \times \mathbf{H} + \mathbf{C}\mathbf{u}_w + \mathbf{T}_c] \\ \dot{\Omega} = \mathbf{J}_w^{-1}\mathbf{u}_w - \mathbf{C}^T\dot{\omega} \end{cases} \quad (7)$$

The kinematics model of the combined spacecraft in terms of the modified Rodrigues parameter (MRP) takes the following form:

$$\dot{\sigma} = \mathbf{G}(\sigma)\omega \quad (8)$$

where  $\sigma = [\sigma_1, \sigma_2, \sigma_3]^T$ , the kinematics matrix  $\mathbf{G}(\sigma)$  is given explicitly by Ref. [24]:

$$\mathbf{G}(\sigma) = \frac{1}{4}[(1 - \sigma^T\sigma)\mathbf{E}_3 + 2\sigma^\times + 2\sigma\sigma^T] = \frac{1}{4}\mathbf{A} \quad (9)$$

$$\mathbf{G}^{-1}(\sigma) = \frac{16}{(1 + \sigma^T\sigma)^2}\mathbf{G}(\sigma)^T = \frac{4}{(1 + \sigma^T\sigma)^2}\mathbf{A}^T \quad (10)$$

where

$$[\sigma^\times] = \begin{bmatrix} 0 & -\sigma_3 & \sigma_2 \\ \sigma_3 & 0 & -\sigma_1 \\ \sigma_2 & \sigma_1 & 0 \end{bmatrix} \quad (11)$$

$$\mathbf{A} = \begin{bmatrix} 1 + \sigma_1^2 - \sigma_2^2 - \sigma_3^2 & 2(\sigma_1\sigma_2 - \sigma_3) & 2(\sigma_3\sigma_1 + \sigma_2) \\ 2(\sigma_1\sigma_2 + \sigma_3) & 1 + \sigma_2^2 - \sigma_3^2 - \sigma_1^2 & 2(\sigma_2\sigma_3 - \sigma_1) \\ 2(\sigma_3\sigma_1 - \sigma_2) & 2(\sigma_2\sigma_3 + \sigma_1) & 1 + \sigma_3^2 - \sigma_1^2 - \sigma_2^2 \end{bmatrix} \quad (12)$$

### 2.3. Contact detection algorithm and contact dynamics model

Select a proper grasping structure is very important to target capture. The existing target projects are investigated to select a suitable grasping structure. They include the apogee motor injector, docking ring and satellite bracket. Among them, bracket is with the characteristics of wide use, simple geometric structure, and full research [26,27]. Therefore, the satellite bracket is selected.

When the end-effector of the space robot performs a target capture process, it will inevitably collide with the target, as illustrated in Fig. 2.

**Assumption 2.** The known manipulator is in the pre-capture configuration and is locked in that configuration after the capture is completed.

The claw is mainly composed of two collapsible hands, namely the  $a_0a_1a_2$  and  $b_0b_1b_2$ . Due to mechanical constraints, the collision may occur multiple times. The contact detection algorithm defined as the non-uniplanar lines distance  $\delta_i = 0$ ,  $\delta_i$  is given by:

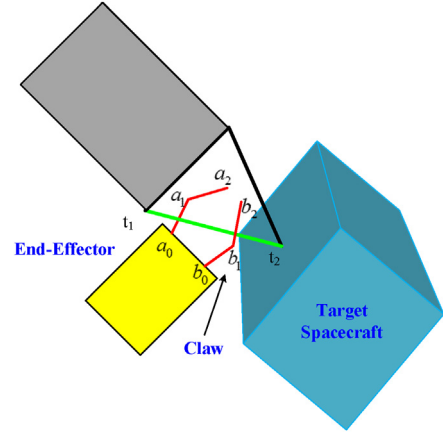


Fig. 2. Illustration of target capturing process.

$$\delta_i = \frac{|(\mathbf{s}_i \times \mathbf{s}_b) \cdot \mathbf{l}_i|}{\|\mathbf{s}_i \times \mathbf{s}_b\|} \quad i = 1, 2, 3, 4 \quad (13)$$

where  $\mathbf{s}_i$  is the vector of claw. Here  $\mathbf{s}_i = [a_0a_1, a_1a_2, b_0b_1, b_1b_2]$ ;  $\mathbf{s}_b = [t_1t_2]$  is the bracket vector, which can be provided by a vision system;  $\mathbf{l}_i = [t_1a_0, t_1a_1, t_2b_0, t_2b_1]$  is the intersection vector.  $a_0, a_1, a_2, b_0, b_1, b_2$  and  $t_1, t_2$  are known or identifiable reference points [27], each element of  $\mathbf{s}_i, \mathbf{s}_b, \mathbf{l}_i$  is a vector linking the two reference points.

The Kelvin model includes contact detection, which is used to model the contact process:

$$\mathbf{F}_{ci} = k_g\delta\mathbf{n} + k_c\dot{\delta}\mathbf{n} \quad (14)$$

where  $k_g$  is the contact stiffness coefficient,  $k_c$  is the contact damping coefficient,  $\dot{\delta}_i$  is the rate of change of the  $\delta_i$  and  $\mathbf{n}$  is the unit vector of the common normal line at the contact point.

$$k_c = 2\xi\sqrt{k_g\frac{m_1m_2}{m_1+m_2}} \quad (15)$$

$$\xi = -\frac{\ln e}{\sqrt{\pi^2 + (\ln e)^2}} \quad (16)$$

where  $e$  is the restitution coefficient. The relationship between the forces  $\mathbf{F}_{ti}$  on the target and forces  $\mathbf{F}_{ci}$  on the space robot is as follows:

$$\mathbf{F}_{ti} = -\mathbf{F}_{ci} \quad (17)$$

Defining the relative position between the contact point and the centroid of space robot as  $\mathbf{d}_r$ , the contact torque can be obtained:

$$\mathbf{T}_{ci} = \mathbf{d}_r \times \mathbf{F}_{ci} \quad (18)$$

Similarly, the torque on the target caused by the contact is given by:

$$\mathbf{T}_{ti} = \mathbf{d}_t \times \mathbf{F}_{ti} \quad (19)$$

where  $\mathbf{d}_t$  denotes the relative position between the contact point and the centroid of target.

### 3. Stability control system design for combined spacecraft

Collision is characterized by the unpredictable contact position and uncertainty of environmental variables. Furthermore, after capturing the target, the formed combined spacecraft has different mass parameters. These conditions bring a great challenge to the attitude control of the combined spacecraft. Based on the control redistribution technique and sliding mode control method, this paper proposes a dual-integral sliding mode control system to achieve the attitude stability of the combined spacecraft, as shown in Fig. 3.

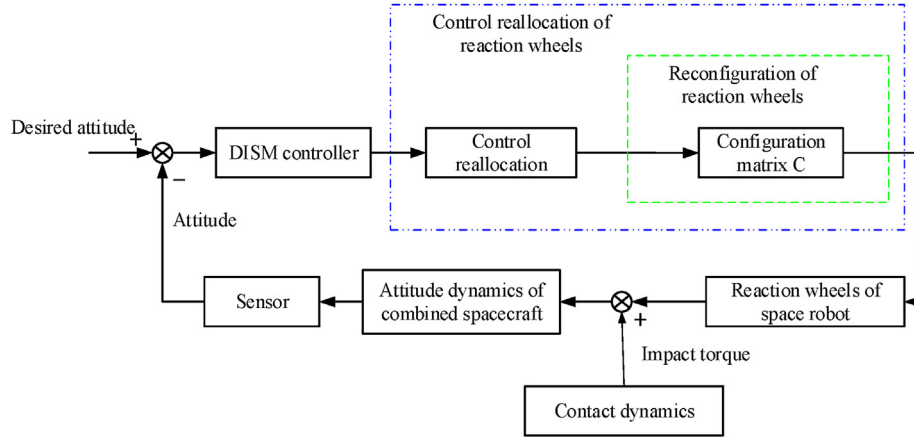


Fig. 3. Block diagram of the stability control system.

### 3.1. Conventional sliding mode controller design

Considering that the attitude controller is designed in the state space, Eqs. (7) and (8) need to be transformed into the state space form.

$$\begin{cases} \dot{\sigma} = G(\sigma)\omega \\ \dot{\omega} = f(\omega) + \mathbf{P}\mathbf{u} + \mathbf{T} \end{cases} \quad (20)$$

where  $f(\omega) = \mathbf{J}_s^{-1}(\omega \times \mathbf{H})$ ,  $\mathbf{P} = \mathbf{J}_s^{-1}$ ,  $\mathbf{u} = \mathbf{C}\mathbf{u}_w$ ,  $\mathbf{T} = \mathbf{J}_s^{-1}\mathbf{T}_c$ ,  $\|\mathbf{T}\| \leq D$  and  $D$  is the upper bound of disturbance.

The attitude error is defined as  $\sigma_e = \sigma - \sigma_d$ , where  $\sigma_d$  is the desired attitude, then the sliding manifold ( $\mathbf{s} = \mathbf{0}$ ) is given by:

$$\mathbf{s} = \omega - m(\sigma) \quad (21)$$

where

$$m(\sigma) = \mathbf{G}^{-1}(\sigma)\Lambda\sigma_e \quad (22)$$

where  $\Lambda$  is a diagonal matrix with negative elements. This allows for decoupled sliding motions and convergence towards the final desired orientation. Taking the derivative of the sliding mode function  $\mathbf{s}$  with respect to the time is given by Refs. [28]:

$$\dot{\mathbf{s}} = \hat{f}(\sigma, \mathbf{s}) + f(\omega) + \mathbf{P}\mathbf{u} + \mathbf{T} \quad (23)$$

where

$$\hat{f}(\sigma, \mathbf{s}) = -\frac{\partial \mathbf{m}}{\partial \sigma} \mathbf{G}(\sigma)(\mathbf{s} + \mathbf{m}(\sigma)) \quad (24)$$

According to the sliding mode function  $\mathbf{s}$  and the upper bound of  $\mathbf{T}$ , we can design the following controller

$$\mathbf{u} = -\mathbf{P}^{-1} \left\{ f(\omega) - \frac{\partial \mathbf{m}}{\partial \sigma} [\mathbf{G}(\sigma)\mathbf{s} + \mathbf{G}(\sigma)\mathbf{m}(\sigma)] + k_s \mathbf{s} + \eta \operatorname{sgn}(\mathbf{s}) \right\} \quad (25)$$

It is noted that  $k_s > 0$  and  $\eta > D$ , they are the design parameters to be determined to ensure the system stability. Substituting the sliding mode controller Eq. (25) into Eq. (23) yields:

$$\dot{\mathbf{s}} = -k_s \mathbf{s} - \eta \operatorname{sgn}(\mathbf{s}) + \mathbf{T} \quad (26)$$

We choose a Lyapunov function as:

$$V(\mathbf{s}) = \frac{1}{2} \mathbf{s}^T \mathbf{s} \quad (27)$$

Taking the derivative of the Lyapunov function with respect to the time, we obtain:

$$\dot{V} = \mathbf{s}^T \dot{\mathbf{s}} = -k_s \mathbf{s}^T \mathbf{s} - |\mathbf{s}^T \mathbf{T}| \eta + \mathbf{s}^T \mathbf{T} \leq 0 \quad (28)$$

According to the LaSalle invariance theory, the closed-loop system is asymptotically stable. The convergence speed of the system depends on  $k_s$ .

When the desired modified Rodrigues parameters  $\sigma_d = 0$ , and the  $\Lambda$  matrix in Eq. (22) is assumed to be given by a scalar  $\lambda$  times the identity matrix, the attitude error function  $\mathbf{m}(\sigma)$  and the attitude partial derivation function  $\frac{\partial \mathbf{m}}{\partial \sigma}$  are given by Ref. [28]:

$$m(\sigma) = 4\lambda(1 + \sigma^T \sigma)^{-1} \sigma \quad (29)$$

$$\frac{\partial m}{\partial \sigma} = 4\lambda(1 + \sigma^T \sigma)^{-1} \{ \mathbf{E}_{3 \times 3} - 2(1 + \sigma^T \sigma)^{-1} \sigma \sigma^T \} \quad (30)$$

The conventional sliding mode control method has certain robustness, and can achieve the adjustment of the attitude deviation and the angular velocity tracking, as depicted in Fig. 4. However, it should be noted that since the angular velocity is not obtained by the attitude angle derivation, the control method cannot directly control the transient attitude response of the space robot, such conditions make the method unsuitable for multiple impacts.

### 3.2. Improved sliding mode controller design

In this section, a dual-integral sliding mode control method is designed to effectively control the instantaneous change of attitude after collision. Considering the different time scales of the attitude angle and attitude angular velocity, the attitude dynamics equation can be decomposed into a fast-subsystem and a slow-subsystem, respectively. The inner loop and outer loop are controlled separately. In the inner loop, a virtual control is designed to force the angular velocity error tracking the virtual control item. In the outer loop, the integral sliding mode is used to realize the tracking of the attitude angle, a diagram of the structure of the control system is depicted in Fig. 5.

Considering the attitude error dynamic Eq. (20), an outer loop integral sliding variable is chosen, then:

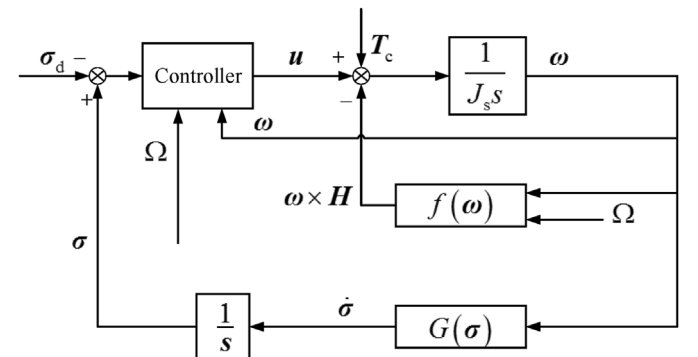


Fig. 4. Block diagram of the conventional sliding mode control.

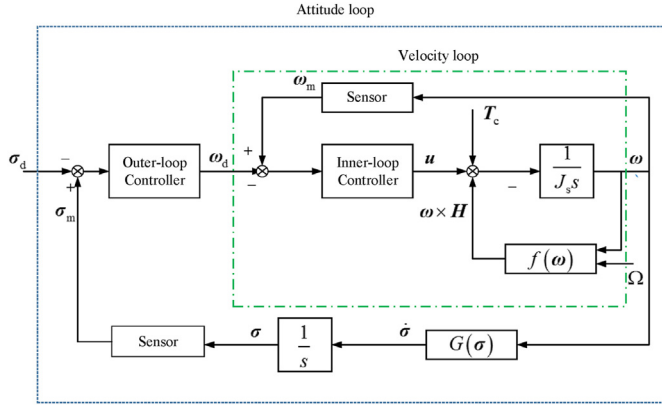


Fig. 5. Block diagram of the improved sliding mode controller.

$$\mathbf{s}_0 = \boldsymbol{\sigma}_e + \mathbf{K}_1 \int_0^t \boldsymbol{\sigma}_e d\tau, \quad \mathbf{s}_0 \in \mathbb{R}^3 \quad (31)$$

where  $\mathbf{K}_1 = \text{diag}([k_{11}, k_{12}, k_{13}])$  is the gain matrix. By selecting the appropriate gain matrix, the state trajectories move onto a sliding manifold.

In Eq. (20),  $\dot{\boldsymbol{\sigma}} = \mathbf{G}(\boldsymbol{\sigma})\boldsymbol{\omega}_d$  is taken, where  $\boldsymbol{\omega}_d$  is the virtual control item, which can be expressed as:

$$\boldsymbol{\omega}_d = \mathbf{G}^{-1}(\boldsymbol{\sigma})(\dot{\boldsymbol{\sigma}}_d - \mathbf{K}_1 \boldsymbol{\sigma}_e) - \mathbf{G}^{-1}(\boldsymbol{\sigma})\rho_1 \text{sgn}(\mathbf{s}_0) \quad (32)$$

where  $\rho_1 > 0$ ,  $\text{sgn}(\mathbf{s}_0) = [\text{sgn}(s_1) \text{sgn}(s_2) \text{sgn}(s_3)]^T$ .

Taking the time derivative of  $\mathbf{s}_0$  in Eq. (31) and using Eq. (20) yields

$$\dot{\mathbf{s}}_0 = \dot{\boldsymbol{\sigma}}_e + \mathbf{K}_1 \boldsymbol{\sigma}_e = \dot{\boldsymbol{\sigma}} - \dot{\boldsymbol{\sigma}}_d + \mathbf{K}_1 \boldsymbol{\sigma}_e = \mathbf{G}(\boldsymbol{\sigma})\boldsymbol{\omega}_d - \dot{\boldsymbol{\sigma}}_d + \mathbf{K}_1 \boldsymbol{\sigma}_e \quad (33)$$

The error between  $\boldsymbol{\omega}$  and  $\boldsymbol{\omega}_d$  is eliminated by the inner loop, that is, the following formula holds:

$$\lim_{t \rightarrow \infty} \|\boldsymbol{\omega} - \boldsymbol{\omega}_d\| = 0 \quad (34)$$

Using the integral sliding surface, the inner sliding function is given by

$$\mathbf{s}_i = \boldsymbol{\omega}_e + \mathbf{K}_2 \int_0^t \boldsymbol{\omega}_e d\tau, \quad \mathbf{s}_i \in \mathbb{R}^3 \quad (35)$$

where  $\boldsymbol{\omega}_e = \boldsymbol{\omega} - \boldsymbol{\omega}_d$ ,  $\mathbf{K}_2 = \text{diag}([k_{21}, k_{22}, k_{23}])$  is the gain matrix.

The inner loop control law  $\mathbf{u}$  is calculated as follows:

$$\mathbf{u} = -\mathbf{P}^{-1}[f(\boldsymbol{\omega}) - \dot{\boldsymbol{\omega}}_d + \mathbf{K}_2 \boldsymbol{\omega}_e + \eta \mathbf{s}_i + \rho_2 \text{sgn}(\mathbf{s}_i)] \quad (36)$$

where  $\rho_2 > D$  and  $\eta > 0$ .

Taking the time derivative of  $\mathbf{s}_i$  in Eq. (35) and using Eq. (20) yields:

$$\dot{\mathbf{s}}_i = \dot{\boldsymbol{\omega}}_e + \mathbf{K}_2 \boldsymbol{\omega}_e = \dot{\boldsymbol{\omega}} - \dot{\boldsymbol{\omega}}_d + \mathbf{K}_2 \boldsymbol{\omega}_e = f(\boldsymbol{\omega}) + \mathbf{P}\mathbf{u} + \mathbf{T} - \dot{\boldsymbol{\omega}}_d + \mathbf{K}_2 \boldsymbol{\omega}_e \quad (37)$$

Proof. Considering the Lyapunov function:

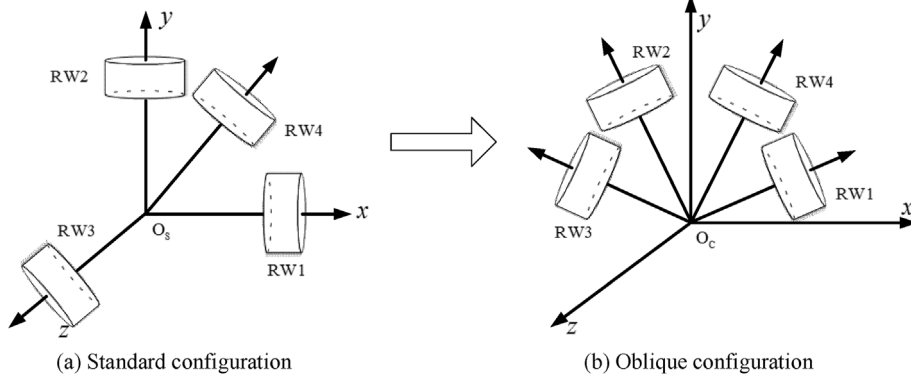


Fig. 6. Configuration of the reaction wheels in different frame conditions.

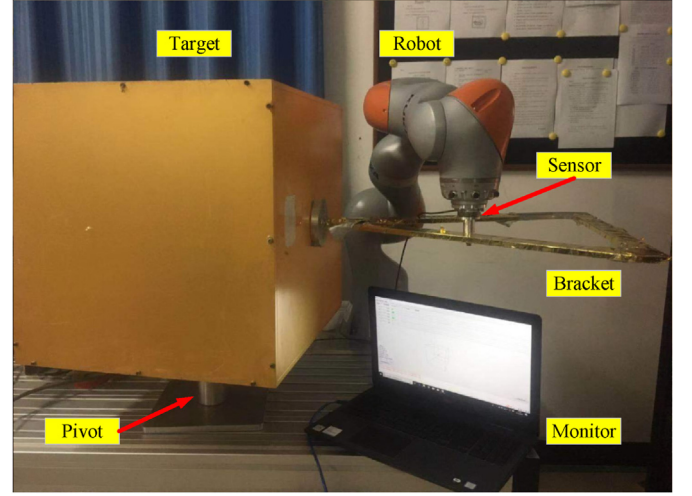


Fig. 7. Experimental setup.

$$V_1(t) = \frac{1}{2} \mathbf{s}_0^T \mathbf{s}_0 \quad (38)$$

Differentiating  $V_1$  with respect to time along the solution of Eq. (33) gives:

$$\begin{aligned} \dot{V}_1 &= \mathbf{s}_0^T \dot{\mathbf{s}}_0 = \mathbf{s}_0^T (\mathbf{G}(\boldsymbol{\sigma})\boldsymbol{\omega}_d - \dot{\boldsymbol{\sigma}}_d + \mathbf{K}_1 \boldsymbol{\sigma}_e) \\ &= \mathbf{s}_0^T (\mathbf{G}(\boldsymbol{\sigma})\mathbf{G}^{-1}(\boldsymbol{\sigma})(\dot{\boldsymbol{\sigma}}_d - \mathbf{K}_1 \boldsymbol{\sigma}_e - \rho_1 \text{sgn}(\mathbf{s}_0)) - \dot{\boldsymbol{\sigma}}_d + \mathbf{K}_1 \boldsymbol{\sigma}_e) \\ &= -\rho_1 \mathbf{s}_0^T \text{sgn}(\mathbf{s}_0) = -\rho_1 \sum_{i=1}^3 |s_i| < 0 \end{aligned} \quad (39)$$

Let the inner loop Lyapunov function be  $V_2(t) = \frac{1}{2} \mathbf{s}_i^T \mathbf{s}_i$ . If the control law  $\mathbf{u}$  is chosen as Eq. (36), with  $\mathbf{s}_i$  in Eq. (35), we obtain:

$$\begin{aligned} \dot{V}_2 &= \mathbf{s}_i^T \dot{\mathbf{s}}_i = \mathbf{s}_i^T (f(\boldsymbol{\omega}) + \mathbf{P}\mathbf{u} + \mathbf{T} - \dot{\boldsymbol{\omega}}_d + \mathbf{K}_2 \boldsymbol{\omega}_e) \\ &= \mathbf{s}_i^T \{f(\boldsymbol{\omega}) - [f(\boldsymbol{\omega}) - \dot{\boldsymbol{\omega}}_d + \mathbf{K}_2 \boldsymbol{\omega}_e + \eta \mathbf{s}_i + \rho_2 \text{sgn}(\mathbf{s}_i)] + \mathbf{T} - \dot{\boldsymbol{\omega}}_d + \mathbf{K}_2 \boldsymbol{\omega}_e\} \\ &= -\eta s^2 - \rho_2 |\mathbf{s}^T| + \mathbf{s}^T \mathbf{T} \leq 0 \end{aligned} \quad (40)$$

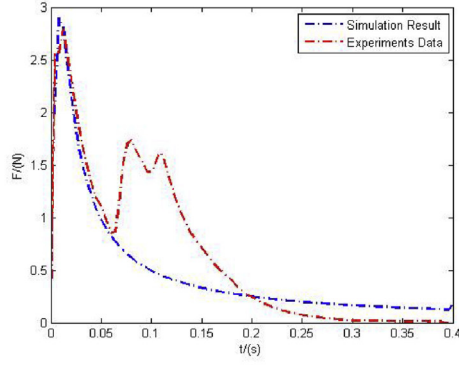
Eq. (38) and Eq. (40) clearly indicate that the controlled system is energy dissipative. Therefore, the proposed control law Eq. (36) can guarantee the stability of the closed-loop system.

The saturation function is used to minimize the chattering in the control torques. This function is defined by:

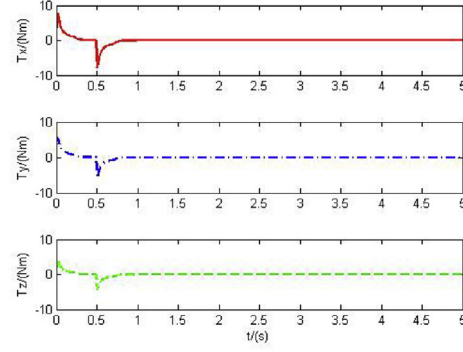
$$\text{sat}(s_i, \varepsilon) = \begin{cases} 1 & \text{for } s_i > \varepsilon \\ \frac{s_i}{\varepsilon} \text{ for } |s_i| \leq \varepsilon - 1 & \\ -1 & \text{for } s_i < -\varepsilon \end{cases} \quad i = 1, 2, 3 \quad (41)$$

where  $\varepsilon$  is a small positive number.





(a) Collision Experiments in the x Direction



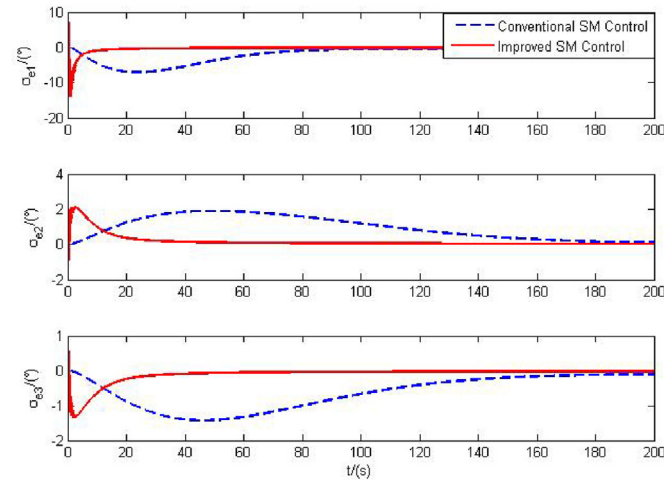
(b) Collision Simulation in Three Directions

Fig. 8. Comparisons of experimental and simulation contact forces.

Table 1

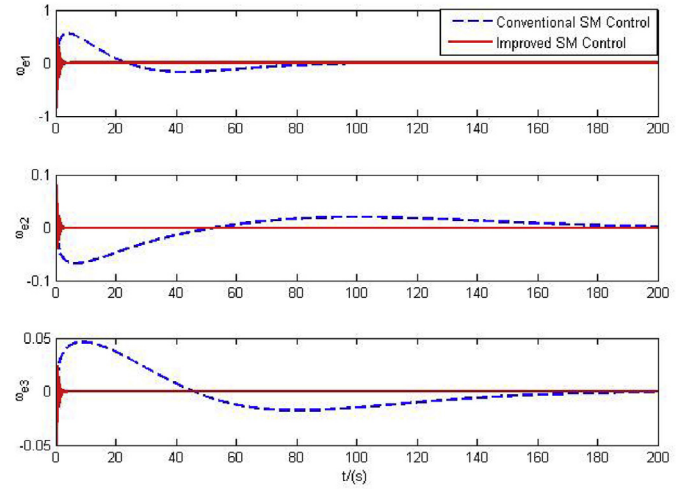
Dynamic parameters of the combined spacecraft system.

Body	Parameter	Unit	Value
Space Robot	$m_S$	kg	1080
	$I_S$	kg-m <sup>2</sup>	diag (405, 405, 405)
Target Spacecraft	$m_T$	kg	675
	$I_T$	kg-m <sup>2</sup>	[245.3, -100, -85; -100, 45.3, -120; -85, -120, 245.3]
Link 1	$m_1$	kg	18.56
	$I_1$	kg-m <sup>2</sup>	diag (0.03, 0.73, 0.73)
	$c_1$	m	(0.3, 0.0, 0.0)
Link 2	$I_1$	m	(0.6, 0.0, 0.0)
	$m_2$	kg	18.56
	$I_2$	kg-m <sup>2</sup>	diag (0.03, 0.73, 0.73)
Link 3	$c_2$	m	(0.3, 0.0, 0.0)
	$I_2$	m	(0.6, 0.0, 0.0)
	$m_3$	kg	18.56
	$I_3$	kg-m <sup>2</sup>	diag (0.03, 0.73, 0.73)
	$c_3$	m	(0.3, 0.0, 0.0)
	$I_3$	m	(0.6, 0.0, 0.0)

Fig. 9. Comparison of the Attitude Errors  $\sigma_e$  with RPY parameters.

### 3.3. Control redistribution based on the Moore-Penrose inverse method

As a result of the post-capture of the target spacecraft using a space robot to form a combined spacecraft, the orthogonal configuration of four reaction wheels in the body coordinate of space robot will become the oblique configuration in the inertia principal axis coordinate of combined spacecraft, “oblique” does not physically reallocates the reaction wheel in structural characteristics, but reconstitutes its

Fig. 10. Comparison of the angular velocity errors  $\omega_e$ .

configuration matrix to adapt to changes in mass characteristic parameters after the formation of a combined spacecraft. This requires redistribution of the reaction wheel control torque, as shown in Fig. 6. The control torque redistribution problem refers to the output of each actuator, which minimizes the objective function according to the desired control result under the constraint conditions. Various control allocation schemes for robotic systems have been studied in the literature, such as the daisy chaining methodology, direct allocation methodology and generalized inverse methodology, etc [29]. As a kind of generalized inverse method, the Moore-Penrose inverse approach has the characteristics of optimal output distribution, which can effectively improve the dynamic performance of the system.

Since control allocation contributes to distributing the control torques effectively, the objective function we adopt in this study is minimizing the control torque  $\mathbf{u}_w$ , and the objective function is given by:

$$J = \min_{\mathbf{u}_w} \|\mathbf{u}_w\|_l \quad \text{s.t. } \mathbf{u} = \mathbf{C}\mathbf{u}_w \quad (42)$$

where  $l$  is the vector norm.

For the control allocation problem described in Eq. (42), the 1-norm allocation model can be used to perform the control task with as few actuators as possible, but often saturates the actuator. The 2-norm allocation model can effectively distribute the desired amount of control to each actuator. Furthermore, the solution of the 2-norm is continuous and unique. Therefore, in this section a 2-norm allocation model is used for optimization.

The 2-norm objective function  $J$  is given by:

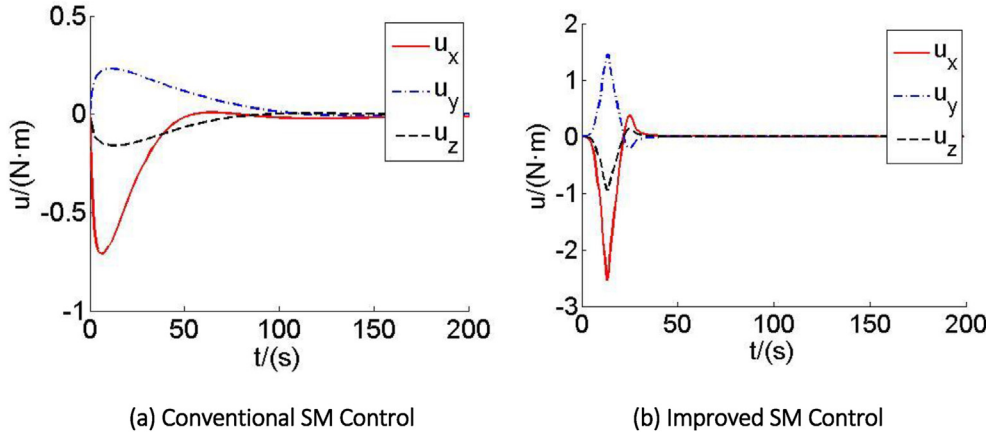


Fig. 11. Comparison of the control torques  $u_c$  of the combined spacecraft.

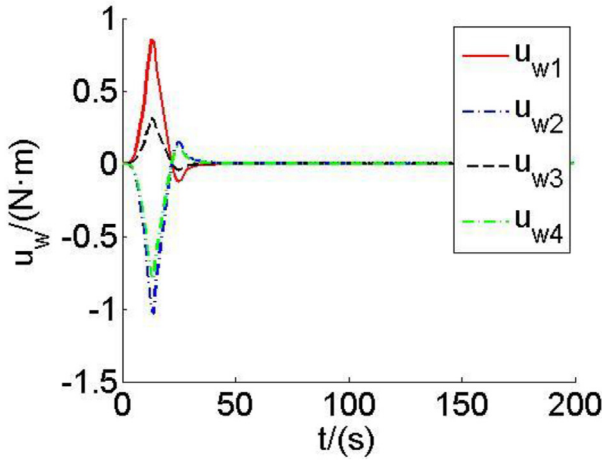


Fig. 12. Control torques  $u_w$  of the reaction wheel.

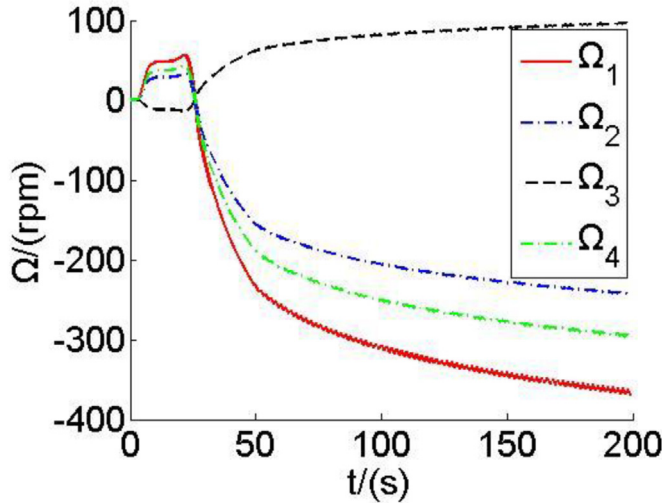


Fig. 13. Speed  $\Omega$  of the reaction wheel.

$$J = \min_{\mathbf{u}_w} \|\mathbf{u}_w\|_2 \quad (43)$$

s.t.  $\mathbf{u} = \mathbf{C}\mathbf{u}_w$

According to Eq. (43), the control torque satisfies the minimum sum of the squares of all elements, and the constraint must be met. Thus, the necessary condition for an optimal control  $\mathbf{u}_w$  is to maximize the following Pontryagin Hamiltonian:

$$H(\mathbf{u}_w, \lambda) = \frac{1}{2} \mathbf{u}_w^T \mathbf{u}_w + \lambda^T (\mathbf{C}\mathbf{u}_w - \mathbf{u}) \quad (44)$$

where  $\lambda$  is the vector of costate variables. Then, the necessary conditions for the solution can be written as follows:

$$\frac{\partial H}{\partial \mathbf{u}_w} = \mathbf{u}_w^T - \lambda^T \mathbf{C} = 0 \quad (45)$$

$$\frac{\partial H}{\partial \lambda} = \mathbf{C}\mathbf{u}_w - \mathbf{u} = 0 \quad (46)$$

Thus, it can be said that

$$\mathbf{u}_w = \mathbf{C}^T (\mathbf{C}\mathbf{C}^T)^{-1} \mathbf{u} = \mathbf{C}^\dagger \mathbf{u} \quad (47)$$

where  $\mathbf{C}^\dagger = \mathbf{C}^T (\mathbf{C}\mathbf{C}^T)^{-1}$  is the Moore-Penrose inverse of matrix  $\mathbf{C}$ .

#### 4. Experiments and numerical simulations

In this section, the physical experiment platform was designed to verify the accuracy of the contact dynamics model, as shown in Fig. 7. A 7 degree-of-freedom (DOF) robotic arm LBR iiwa made by KUKA, was used as a manipulator of a space robot. A rigid rod was mounted on the end tip of LBR iiwa with 6-axis force/torque sensor NetFT made by ATI Industrial Automation corporation, it is used to simulate a colliding finger in the multi-finger claw.

The ATI NetFT sensor was used with a transmission rate of 500 Hz and a typical gain error of less than 0.5%, that can meet the real-time and reliability requirements of F/T value detection. We install it at the end of the robot arm to collect collision F/T information, this information is used to compare with simulation results based on contact dynamics model. The data obtained from the measurement is transmitted to the host computer for display and storage via the network, it includes header, number, F/T measurement result and measurement time.

A satellite model was mounted on the pivot as a rotating target, it is capable of emulating a one dimensional smooth motion utilizing the pivot with negligibly small friction. A bracket was mounted on the satellite model as a grasping structure, it was made of aluminum and could rotated by 8 deg/s. A laser encoder was attached to the pivot to sense the model angular velocity.

The pre-contact relative velocity was 0.8 cm/s, where the bracket approached the manipulator at 0.8 cm/s. The impact force was measured by NetFT sensor and was stored into the monitor in text file format. To verify the accuracy of the contact dynamics model, we use MATLAB R2015a for simulation research based on Eq. (14). The parameters of simulation were selected as  $k_g = 2.3549 \times 10^4 \text{ N/m}$ ,  $k_c = -276.4238 \text{ N/(m/s)}$ ,  $m_1 = 675 \text{ kg}$ ,  $m_2 = 1080 \text{ kg}$ ,  $v_s = 0.07 \text{ cm/s}$ , where  $m_1$  is the mass of the target,  $m_2$  is the mass of the space robot, and  $v_s$  is the relative velocity. The comparison between the experimental results and the simulation results is shown in Fig. 8(a). We calculated the root

mean square error (RMSe)  $r = 0.0356$ , which demonstrated that the contact model and parameters selection were accurate. After 0.05 s, the experimental data increased again because the experimental robot is on a fixed base, and the rebound after the collision causes the occurrence of a secondary contact, which is an inherent error of the system and does not affect the reliability of the experimental results.

Using the experimentally modified collision model and contact detection algorithm, we simulated the multiple impacts in a three-dimensional space. The relative velocity  $\mathbf{v}_0 = [0.029, 0.021, 0.016]^T \text{ m/s}$  is based on already available research results [30], and the results are shown in Fig. 8(b). Due to the mechanical limitation of the claw, multiple impacts occurred during the capture, the contact time was less than 1s, and the maximum contact torque was 7.718 Nm. The simulation results showed that the collisions have the characteristics of short time and large torque. The design of the controller under the condition of limited output control torque is a great challenge.

In order to verify the effectiveness of the proposed control method, the three-link manipulator was adopted as shown in Table 1, the joints of the manipulator are locked at  $\theta = [-10^\circ 35^\circ 60^\circ]$ .

The inertial matrix  $\mathbf{I}$  and the configuration  $\mathbf{C}$  of reaction wheels in the inertia principal axis frame  $O_C x_C y_C z_C$  of the combined spacecraft are individually calculated:

$$\mathbf{I} = \begin{bmatrix} 672.9 & 0 & 0 \\ 0 & 4002.5 & 0 \\ 0 & 0 & 4238.9 \end{bmatrix} \text{ and } \mathbf{C} = \begin{bmatrix} -0.9992 & -0.0300 & -0.0256 & -0.6086 \\ -0.0394 & 0.7455 & 0.6653 & 0.7913 \\ 0.0009 & -0.6658 & 0.7461 & 0.0469 \end{bmatrix}$$

The reaction wheel control torque redistribution matrix is calculated as:

$$\mathbf{C}^\dagger = \begin{bmatrix} -0.8236 & -0.2679 & -0.0127 \\ 0.1457 & 0.5171 & -0.6794 \\ 0.1501 & 0.4369 & 0.7326 \\ -0.3045 & 0.3959 & 0.0235 \end{bmatrix}$$

Without losing generality, the initial attitude angle, initial angular velocity, expected attitude angle and expected angular velocity are assumed to be set to zero. The single reaction wheel has an inertia of  $0.338 \text{ kg m}^2$ , maximum speed of 500 rpm, maximum angular momentum of 17.8 Nm, and maximum output torque of 1 Nm. The simulation time is 200 s. The designed parameters are respectively  $\mathbf{K}_1 = \text{diag}([0.5, 0.3, 0.3])$ ,  $\mathbf{K}_2 = \text{diag}([3, 1.8, 1.8])$ ,  $\rho_1 = 5$ ,  $\rho_2 = 20$ ,  $\eta = 3$ , and  $\varepsilon = 0.1$ . Then, the traditional sliding mode control and the improved sliding mode control are respectively used to achieve the stability control after collision, and the two are compared and analyzed.

The comparison of the Euler angle variation curve of the attitude error  $\sigma_e$  is shown in Fig. 9, the comparison of the angular velocity error  $\omega_e$  is shown in Fig. 10, and the output characteristic curve of the control torque  $\mathbf{u}_c$  is shown in Fig. 11. The dual-loop integral sliding mode controller is used to direct the control the state variable  $\omega$ , which improves the capability of the control transient attitude response. As can be seen, both the attitude error and the angular velocity error converge to zero after 50 s. Compared with the traditional sliding mode controller, it can efficiently shorten the convergence time.

For the improved sliding mode control, the control torques  $\mathbf{u}_w$  of the reaction wheel is shown in Fig. 12 and the corresponding speed  $\Omega$  of the reaction wheels is shown in Fig. 13. Since the integral method and saturation function are adopted, the control torque output is smooth and has engineering applicability. The reaction wheels control torques that are less than 1Nm, which meet the requirement of the maximum output torque, and the maximum speed of reaction wheel is 350 rpm within the limits  $[-500, 500]$  rpm. Therefore, the attitude control system can not only achieve the stable control of the combined spacecraft after multiple impacts, but also save precious propellant.

## 5. Conclusions

A dual-integral sliding mode control system has been designed for the stability control of a combined spacecraft after multiple impacts during the process of capturing a tumbling target by a space robot. A multiple impact detection algorithm is proposed and applied to the contact dynamics model. The experiments proved the accuracy of the model. Through the reconfiguration of the reaction wheels, the problem of the changing mass characteristics is solved, and the validity of the method is verified by numerical simulation. Compared with the conventional sliding mode controller, the improved sliding mode controller described here effectively shortens the convergence time. In summary, the combined spacecraft stabilization strategy can effectively deal with the multiple impacts in tumbling target capture processes.

## Declaration of competing interest

We declare that submitted manuscript does not contain previously published material, and are not under consideration for publication elsewhere. Each author has made an important scientific contribution to the study and is thoroughly familiar with the primary data. All authors listed have read the complete manuscript and have approved submission of the paper. The manuscript is truthful original work without fabrication, fraud or plagiarism. All authors declare that there are no conflicts of interest.

We would be happy if the manuscript will be evaluated by your Editorial Board members for publication in the *Acta Astronautica*.

## Acknowledgments

This work was supported by the National Natural Science Foundation of China (nos. 61725303).

## References

- [1] X. Chu, Q. Hu, J. Zhang, Path planning and collision avoidance for a multi-arm space maneuverable robot, *IEEE Trans. Aero. Electron. Syst.* 54 (2018) 217–232.
- [2] G. Chen, B. Yuan, Q. Jia, H. Sun, W. Guo, Failure tolerance strategy of space manipulator for large load carrying tasks, *Acta Astronaut.* 148 (2018) 186–204.
- [3] A. Stolfi, P. Gasbarri, M. Sabatini, A parametric analysis of a controlled deployable space manipulator for capturing a non-cooperative flexible satellite, *Acta Astronaut.* 148 (2018) 317–326.
- [4] Y. Jia, A.K. Misra, Trajectory planning for a space robot actuated by control moment gyroscopes, *J. Guid. Contr. Dynam.* 41 (2018) 1833–1841.
- [5] A. Flores-Abad, O. Ma, K. Pham, S. Ulrich, A review of space robotics technologies for on-orbit servicing, *Prog. Aero. Sci.* 68 (2014) 1–26.
- [6] F. Aghili, A prediction and motion-planning scheme for visually guided robotic capturing of free-floating tumbling objects with uncertain dynamics, *IEEE Trans. Robot.* 28 (2012) 634–649.
- [7] R.C. Youngquist, M.A. Nurge, S.O. Starr, F.A. Leve, M. Peck, A slowly rotating hollow sphere in a magnetic field: first steps to de-spin a space object, *Am. J. Phys.* 84 (2016) 181–191.
- [8] N. Ortiz Gómez, S.J.I. Walker, Eddy currents applied to de-tumbling of space debris: analysis and validation of approximate proposed methods, *Acta Astronaut.* 114 (2015) 34–53.
- [9] N. Praly, M. Hillion, C. Bonnal, J. Laurent-Varin, N. Petit, Study on the eddy current damping of the spin dynamics of space debris from the Ariane launcher upper stages, *Acta Astronaut.* 76 (2012) 145–153.
- [10] N.O. Gómez, S.J.I. Walker, Guidance, navigation, and control for the eddy brake method, *J. Guid. Contr. Dynam.* 40 (2017) 52–68.
- [11] D.N. Dimitrov, K. Yoshida, Momentum distribution in a space manipulator for facilitating the post-impact control, 2004, *IEEE/RJS Int. Conf. Intell. Robot. Syst.* 4 (2004) 3345–3350.
- [12] K. Yoshida, N. Sashida, Modeling of impact dynamics and impulse minimization for space robots, *Int. Conf. Intell. Robot. Syst.* (1993) 2064–2069 1993.
- [13] S. Liu, L. Wu, Z. Lu, Impact dynamics and control of a flexible dual-arm space robot capturing an object, *Appl. Math. Comput.* 185 (2007) 1149–1159.
- [14] B. Zhang, B. Liang, Z. Wang, Y. Mi, Y. Zhang, Z. Chen, Coordinated stabilization for space robot after capturing a noncooperative target with large inertia, *Acta Astronaut.* 134 (2017) 75–84.
- [15] A. Stolfi, P. Gasbarri, M. Sabatini, A combined impedance-PD approach for controlling a dual-arm space manipulator in the capture of a non-cooperative target, *Acta Astronaut.* 139 (2017) 243–253.
- [16] A. Flores-Abad, Z. Wei, O. Ma, K. Pham, Optimal control of a space robot to approach a tumbling object for capture with uncertainties in the boundary conditions,



- AIAA Guid. Navig. Control Conf. (2013) 1–13.
- [17] A. Flores-Abad, Z. Wei, O. Ma, K. Pham, Optimal control of space robots for capturing a tumbling object with uncertainties, *J. Guid. Contr. Dynam.* 37 (2014) 2014–2017.
- [18] N. Uyama, T. Narumi, Hybrid impedance/position control of a free-flying space robot for detumbling a noncooperative satellite, *IFAC-PapersOnLine* 49 (2016) 230–235.
- [19] W. He, Y. Dong, C. Sun, Manipulator with input saturation, *IEEE Trans. Syst. Man, Cybern. Syst.* 46 (2016) 334–344.
- [20] X. Cyril, G.J. Jaar, A.K. Misra, Dynamical modelling and control of a spacecraft-mounted manipulator capturing a spinning satellite, *Acta Astronaut.* 35 (1995) 167–174.
- [21] W. Xu, C. Li, B. Liang, Y. Xu, Y. Liu, W. Qiang, Target berthing and base reorientation of free-floating space robotic system after capturing, *Acta Astronaut.* 64 (2009) 109–126.
- [22] C.M. Roithmayr, C.D. Karlgaard, R.R. Kumar, D.M. Bose, Integrated power and attitude control with spacecraft flywheels and control moment gyroscopes, *J. Guid. Contr. Dynam.* 27 (2004) 859–873.
- [23] C. Wei, J. Luo, H. Dai, J. Yuan, J. Xie, Efficient adaptive constrained control with time-varying predefined performance for a hypersonic flight vehicle, *Int. J. Adv. Rob. Syst.* 14 (2017) 1–17.
- [24] P. Huang, M. Wang, Z. Meng, F. Zhang, Z. Liu, Attitude takeover control for post-capture of target spacecraft using space robot, *Aero. Sci. Technol.* 51 (2016) 171–180.
- [25] P. Huang, D. Wang, Z. Meng, F. Zhang, Z. Liu, Impact dynamic modeling and adaptive target capturing control for tethered space robots with uncertainties, *IEEE/ASME Trans. Mech.* 21 (2016) 2260–2271.
- [26] P. Huang, L. Chen, B. Zhang, Z. Meng, Z. Liu, Autonomous rendezvous and docking with nonfull field of view for tethered space robot, *Int. J. Aerosp. Eng.* 2017 (2017).
- [27] L. Chen, P. Huang, J. Cai, Z. Meng, Z. Liu, A non-cooperative target grasping position prediction model for tethered space robot, *Aero. Sci. Technol.* 58 (2016) 571–581.
- [28] J.L. Crassidis, F.L. Markley, Sliding mode control using modified Rodrigues parameters, *J. Guid. Contr. Dynam.* 19 (1996) 1381–1383.
- [29] W.C. Durham, Constrained control allocation, *J. Guid. Contr. Dynam.* 16 (1993) 717–725.
- [30] D. Han, P. Huang, Trajectory prediction of space robot for capturing non-cooperative target, 2017 18th Int. Conf. Adv. Robot. ICAR 2017 (2017) 328–333.